NUMERICAL SIMULATION OF A SOLAR WOOD DRYER

Santiago F. Corzo * [a], Juan Villemur [b], Rodolfo Pienika [b] and Pedro A. Galione [c]

[a]*CIMEC Centro de Investigación de Métodos Computacionales, UNL, CONICET, FICH, Col. Ruta 168 s/n, Predio Conicet "Dr Alberto Cassano", 3000 Santa Fe, Argentina,*
santiagofcorzo@gmail.com*, http://www.cimec.org.ar*

[b]*Institute of Fluid Mechanics and Ambient Engineering (IMFIA), Faculty of Engineering, Universidad de la República, Uruguay. https://www.fing.edu.uy/es/imfia*

[c]*Institute of Mechanical Engineering and Industrial Production (IIMPI), Faculty of Engineering, Universidad de la República, Uruguay. https://www.fing.edu.uy/es/iimpi*

Keywords: Solar kilns, Wood dryer, Airflow characterization, Computational Fluid Dynamics, OpenFOAM.

Abstract. This article addresses a comprehensive analysis of the fluid dynamics in an Oxford-type solar kiln for wood drying. The work focused on a solar dryer located in Tacuarembó (Uruguay) and the approach is both experimental and numerical. A detailed analysis of the internal fluid dynamics in this type of kiln is essential to improve drying efficiency and avoid heterogeneous drying, which can lead to defects such as wood warping and reduced mechanical properties. It is well known and widely analyzed in the literature that ensuring homogeneous flow in the wood castle is crucial to avoid these problems. To address these challenges, an experimental analysis was performed to characterize the flow behavior inside the kiln. Additionally, numerical simulations were performed with OpenFOAM, incorporating a fan model based on data provided by the manufacturer. A rigorous mesh convergence study validated the numerical results with experimental measurements. The simulations revealed key flow characteristics, including stagnation zones, recirculation areas, flow diversion around the stack, and flow heterogeneity within the stack. Potential modifications to the furnace design are proposed to improve flow uniformity and minimize air diversion, leading to improved dryer performance.

LIST OF SYMBOLS

t: Time
U: Velocity
p: Pressure
ρ: density
μ: Dinamic viscosity
k: Turbulence kinetic energy
ω: specific rate of dissipation
v: Measured velocity
P_v: Measured dynamic pressure
Q: Volumetric flow rate
A: Cross-sectional Area
N: Mesh size
a, b, c, n_1, n_2: Mesh parameters
y: Vertical height
Δp: Pressure jump
C_i: Pressure jump polynomial coefficients
f: Frecuency

Acronyms:
CFD: Computational Fluid Dynamics
OpenFOAM: Open Field Operation and Manipulation
RANS: Reynolds Averaged Navier-Stoke
SST: Shear stress tensor
PISO: Pressure Implicit with Splitting of Operator
PIMPLE: Pressure Implicit Method for Pressure-Linked Equations
GAMG: Geometric agglomerated Algebraic MultiGrid preconditioner

1 INTRODUCTION

Timber drying is a fundamental process in the wood industry that involves reducing the moisture content of wood to an optimal level for its intended use. Proper wood drying is crucial as it improves the dimensional stability, mechanical properties, and overall quality of the wood, making it less prone to defects such as warping, splitting, and decay. This process ensures the durability and longevity of the wood products and prepares the wood for further processing and finishing. Although wood drying is a complex process, due to wood being a biological material with high anisotropy and heterogeneity, one of the most important variables in drying is moisture transport in the air. The increase in temperature and the difference in humidity between the air close to the surface of the wood and the circulating bulk air generates a mass transfer potential from the wood to the bulk air. The drying rate will depend on the temperature and humidity conditions achieved in the dryer and the air circulation speed within the stack. Therefore, ensuring adequate airflow with a uniform moisture concentration throughout the wood is crucial [Perré (2007); Perré and Keey (2014); Lamrani et al. (2023)].

A challenge in these systems is achieving homogeneous airflow within the stack to ensure a consistent drying rate of the boards, regardless of their location. Differences in air velocities result in varying convection coefficients. Furthermore, the mass flow of air through each channel is closely related to the moisture variation within it (i.e., incoming air has less humidity than air exiting the stack), with greater differences observed in channels with lower airflow. Significant variations in air moisture along the channels and differences in convection coefficients result in different drying conditions. These differences in the stack create the defects mentioned above in the wood boards, as different humidity gradients result in different internal stresses [Perré (2007); Perré and Keey (2014)].

There are several types of lumber dryers, with "air drying" being the most common. Among solar timber kilns, various designs and configurations are available [Prakash and Kumar (2017)]. In all of them, solar energy is absorbed and converted into heat, typically heating the internal air and the wood stack, instead of heating the air with some fuel (as occurs in industrial dryers). Fans are usually used to force air circulation between the solar energy collector and the wood stack. There are numerous studies in the literature on solar wood dryers, focusing on evaluating their energy performance and/or economic viability, either to optimize design and operation—such as the configuration of the transparent cover [Bekkioui (2021)], or the use of ventilation and air velocity control [Khater et al. (2004)]—or to assess performance under different climatic conditions [Hasan and Langrish (2014)], or compare different dryer types [Hasan and Langrish (2015)]. These studies typically employ global (0D) or one-dimensional energy balance models, using the airflow velocity between the boards as an input to estimate heat and mass transfer coefficients. A common assumption in these models is that the airflow is uniformly distributed throughout the wood stack, with typical velocities being between $0.5 m/s$ [Hasan and Langrish (2015)] and $3 m/s$ [Khater et al. (2004)].

The effect of airflow conditions on drying performance has been analyzed in the literature. Some studies address the issue of non-homogeneous air velocity distribution in the stack [see e.g. Ledig et al. (2007); Zhao and Cai (2017)]. In Haque and Langrish [Haque and Langrish (2001)], the difference in drying between the stack areas located at the beginning and end of the airflow path in an Oxford-type solar dryer is studied, to assess the need to consider this variation in a computational model to minimize the calculation time. In industrial dryers, airflow reversal is used to minimize these drying differences [Perré and Keey (2014)]. Haque and Langrish [Haque and Langrish (2001)] conclude that the differences are insignificant in a solar dryer

operating with temperatures up to $60\,^{\circ}C$ (dry bulb) and $50\,^{\circ}C$ (wet bulb), air velocities in the stack of $1m/s$, and a path length of more than $6m$, suggesting that flow reversal might not be necessary. Hasan and Langrish [Hasan and Langrish (2014)], in a numerical simulation study, mention that Oxford-type solar dryers with an air velocity of $0.5m/s$ between $25mm$ thick boards separated by $20mm$, in various regions of Australia, achieve acceptable levels of internal stress and defects. Furthermore, multiple studies suggest that intermittent drying can be beneficial from an energy savings perspective, associated with a shorter effective drying time (that is, the time the fans are on) compared to continuous drying [Herritsch et al. (2010)]. Solar dryers can take advantage of this characteristic by turning off the fans at night.

Over the years, much knowledge has been acquired in the literature on solar wood timber through computational models and experimental measurements based on prototypes. However, there is a lack of experimental studies that analyze the interior fluid dynamics of a full-scale solar dryer. The present work addresses the study of an Oxford-type [Prins (1981)] solar wood dryer located in Tacuarembó, Uruguay (in the northeast of the country). The equipment is currently used for drying experiments. A Computational Fluid Dynamics (CFD) study using OpenFOAM is conducted, supported by experimental measurements, to understand the fluid dynamics within it and to develop a reliable computational model capable of evaluating future modifications and redesigns to achieve an adequate flow distribution throughout the wood stack. Additionally, this model can be used to assess differences in drying conditions in various sectors of the stack and convection coefficients in the solar collector area for use in 0D or 1D models.

The study is conducted to analyze the fluid dynamics in detail from both an experimental and a numerical simulation approach. Under normal operating conditions, the collector is evaluated with the fans turned on, and velocity and pressure measurements are taken at various points in the wood dryer to assess the capability of computational models. On the other hand, in the numerical simulation, a mesh convergence study is performed to evaluate its accuracy. Once the computational tool is validated, it is used to analyze the flow distribution, identify areas of flow stagnation, and ultimately evaluate possible redesigns aimed at improving the flow distribution between the boards in the stack.

The paper is outlined in the following stages: In section 2 a complete description of the kiln is addressed, in section 3 the mathematical models are described, and in section 4 the main experimental setups are presented. Finally, in section 5 experimental results are presented, numerical validations are carried out, the main characteristics of the fluid dynamics are developed in detail, and finally, possible redesigns to improve the flow homogeneity between timbers are discussed.

2 DESCRIPTION OF THE SOLAR DRYER

The solar dryer is an Oxford-type structure made of wood, which can be divided into two zones (see figure 1): an upper zone that functions as a solar collector and a lower zone where the stack of wood to be dried is located (the drying zone). The device has dimensions of 4.47 m $\times$ 4 m $\times$ 3.2 m in length, width, and height,t, respectively, with a capacity of approximately 5 m^3 of solid wood to be dried. The airflow through the system is generated by two axial fans positioned at the top. The collector zone consists of a channel formed by a transparent polycarbonate upper cover and a black-painted wooden sheet that acts as a solar energy absorber. Air is heated as it passes through this zone and then enters the drying zone, where it exchanges heat and moisture with the stack of wood to be dried. Although the original design appeared to include vents for partial renewal of the internal air, these were not incorporated into the constructed device. Therefore, intentional air renewal can only be achieved by opening the access doors.

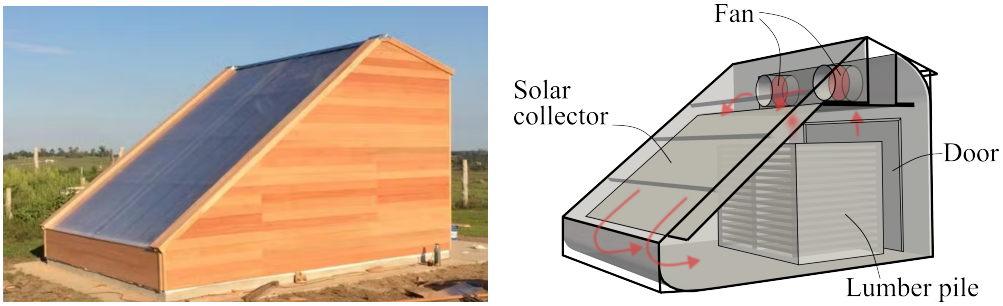

a) *b*)

Figure 1: Sketch of the solar collector.

There are two VEINSA® axial fans, model BHS-P 382 (VEINSA (2024)), each with a diameter of 650 mm, aluminum alloy blades, and a SAE 1020 carbon steel casing protected with synthetic enamel. Each fan is coupled to a three-phase induction motor with a power rating of 1.5 HP and a nominal speed of 1500 rpm, which are driven by a frequency converter, allowing speed adjustment. The normal rotation direction of the fans is set to drive airflow towards the collector zone, but it is possible to reverse the flow direction.

The fan characteristic curve was obtained from the supplier (VEINSA) for the nominal rotation speed. As the characteristic curve of the fan is given in graphical format, it is desirable to represent it with an analytical function. To achieve this, the curve that relates the static pressure Δp (in Pa) with the flow rate $\dot{v}$ (in m^3/s) of the fan working at $50Hz$ is fitted by a third degree polynomial function:

$$\Delta p = 186.7 + 43.25\dot{v} - 50\dot{v}^2 + 6.06\dot{v}^3 \tag{1}$$

Also, since the fans are driven by a variable frequency drive, it is necessary to work with curves that depend on the rotation speed or frequency. So, the theory of similitude is applied in order to relate the static pressure and flow rate at $50Hz$ to those values at any frequency of the converter [Equations (2) and (3)]. In this procedure, the slip in the rotor of the induction motor is assumed to vary proportional to the frequency.

$$\frac{\Delta p_{@f}}{f^2} = \frac{\Delta p_{@50Hz}}{50^2} \tag{2}$$

$$\frac{\dot{v}_{@f}}{f} = \frac{\dot{v}_{@50Hz}}{50} \tag{3}$$

Finally, replacing (2) and (3) in (1), Equation (4) is obtained, relating the static pressure of the fan (in Pa) with the flow rate (in m^3/s) and the frequency (in Hz).

$$\Delta p_{@f} = 0.0747f^2 + 0.865f\dot{v}_{@f} - 50\dot{v}_{@f}^2 + 302.8\frac{\dot{v}_{@f}^3}{f} \tag{4}$$

Fan curves for $50Hz$ (nominal speed) and $40Hz$ (used in the experimental test described in section 4) are presented in Fig. 2.

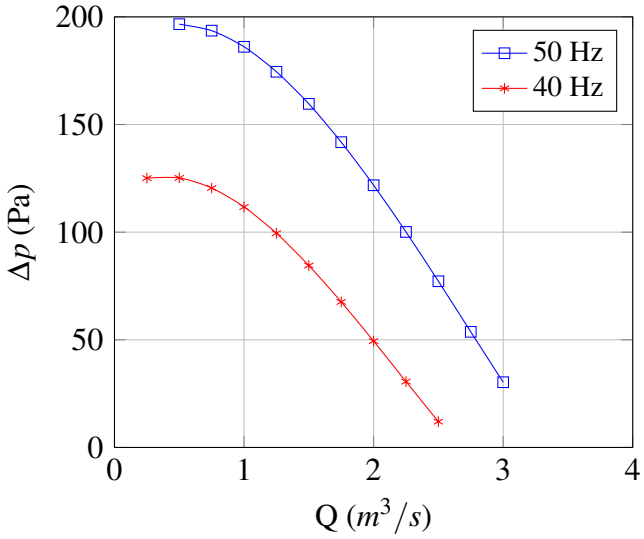

Figure 2: Fan curves for one BHS-P 382 working at 50 Hz and 40 Hz.

3 MATHEMATICAL FORMULATION

The computational model is implemented in the OpenFOAM-8.0 suite (Open Field Operation and Manipulation) Ltd (2020). In this work, all thermophysical properties are considered constant. The governing equations for single-phase incompressible Newtonian flow are given by the Reynolds Averaged Navier-Stokes (RANS) equations (buoyantPimpleFoam solver), which consist of the continuity and momentum equation balance as read:

$$\nabla \cdot (\overline{U}) = 0 \tag{5}$$

The momentum ($UEqn$) is written as:

$$\frac{\partial \overline{U}}{\partial t} + \nabla(\overline{U} \cdot \overline{U}) = -\frac{1}{\rho}\nabla p + \frac{1}{\rho}\nabla \cdot \mu(\nabla \overline{U} + (\nabla \overline{U})^T) - \nabla \cdot (U' \times U') \tag{6}$$

for the mass and momentum equations respectively. The term $U' \times U'$ is the Reynolds stress tensor, which arises from the time- or ensemble-averaged equations. Several models have been developed to estimate this term. One of the most widely used is the Boussinesq eddy viscosity model, which assumes that the Reynolds stress tensor is similar to the laminar stress tensor, but associated with a turbulent viscosity (μ_t). Thus, results in the following form for the momentum equation:

$$\frac{\partial \overline{U}}{\partial t} + \nabla(\overline{U} \cdot \overline{U}) = -\frac{1}{\rho}\nabla p + \frac{1}{\rho}\nabla \cdot \mu_{eff}(\nabla \overline{U} + (\nabla \overline{U})^T) \tag{7}$$

where μ_{eff} is the effective viscosity, which is the sum of the molecular and turbulent viscosities ($\mu_{eff} = \mu + \mu_t$. μ_t), and can be calculated using the eddy viscosity model (closure model). The k-ω SST model is selected due to its versatility to blend the turbulence in the high turbulence in the bulk (using k-ε Launder and Spalding (1983)) and the low turbulence in the boundary layers (using k-ωWilcox (2008)). The SST k-ω model developed by Menter et al. Menter et al. (2003) is the most recommended for industrial applications where precision and computational cost must be balanced.

As shown in Figure 1-b, the fans are considered to be a flat circle in the cylindrical duct's central area. The model treats this circle as a boundary with two surfaces, between which it imposes a pressure jump based on the flow rate (fan characteristic curve). This boundary condition in OpenFOAM is called "fanPressureJump" and it implicitly imposes a pressure jump (Δp) —calculated in terms of the volumetric flow rate ($\dot{v}$)— that is averaged across the surface at each PIMPLE iteration. Rotational effects induced by the fans are neglected.

The pressure jump equation used here —derived from Eq. 4 by fixing $f = 40Hz$— is,

$$\Delta p = C_0 + C_1\dot{v} + C_1\dot{v}^2 + C_2\dot{v}^3 [Pa] \tag{8}$$

where the coefficients are $C_0 = 119.8Pa$, $C_1 = 34,72Pa(s/m^3)$, $C_2 = -49.91Pa(s^2/m^6)$ and $C_3 = 7,544Pa(s^3/m^9)$.

In terms of numerical schemes, a Backward Euler scheme was used for time integration, and first-order linear schemes were used for divergence and gradient terms, except for turbulence fields, for which the upwind scheme was chosen. A corrected linear scheme was used for the Laplacian terms. The "Multigrid" method (GAMG) was chosen to solve the pressure equation and the "SmoothSolver" was chosen for the other linear equation systems. A relative and absolute tolerance of 1×10^{-3} and 1×10^{-9} respectively was considered for the convergence of the linear system. 12 iterations were performed in the outer PIMPLE loop and 10 iterations for the PISO loop. PIMPLE residual controls of 1×10^{-2} and 1×10^{-9} were specified for the relative and absolute residuals. The velocity results were obtained by time averaging the fields after running enough time to reach steady-state flow conditions.

4 EXPERIMENTAL SETUP AND TEST

The experimental test involves operating the fans at a frequency of 40 Hz with the dryer empty (without the stack of wood), measuring the airflow rate in the collector zone and the velocity at various points within the drying zone (see fig. 3-a), as well as the static pressure difference between the fan inlet and outlet. The sky conditions were very cloudy, and the temperature differences between the solar collector absorber surface and the air were very low.

4.1 Instruments and Measurement Methods

To determine the velocities in the section of the solar collector zone (view fig. 3-a), and thus the flow rate, an NPL-type Pitot tube (ellipsoidal nose) with a diameter of 8 mm was positioned at 25 points within a cross-sectional area, distributed according to ISO 3966 standards (see fig. 3-b). With the same instrument, velocities in the main section at a distance of 1 and 2 m (L_1 and L_2) from the collector outlet are measured at various heights, as shown in fig. 3-a.

Dynamic pressures were acquired using a SUPERIOR SENSOR differential micromanometer, model HV110, with an uncertainty of 0.1% of the full scale, set to 125 Pa in this case. Using Equation 9, velocities corresponding to each measurement point were calculated,

$$v = \sqrt{\frac{2P_v}{\rho}} \tag{9}$$

where P_v is the measured dynamic pressure, and ρ is the air density.

The representative velocity for the section $\bar{v}$ is calculated as the arithmetic mean of these measurements, and the flow rate Q is determined using $Q = \bar{v}A$, where A is the cross-sectional area of the duct.

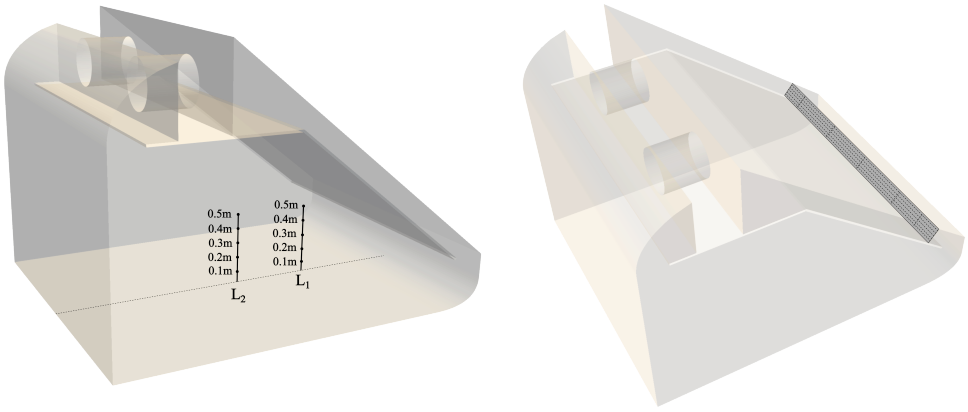

a)Left: $L_1 = 1\,\text{m}$ and $L_2 = 2\,\text{m}$. Right: cross-section location.

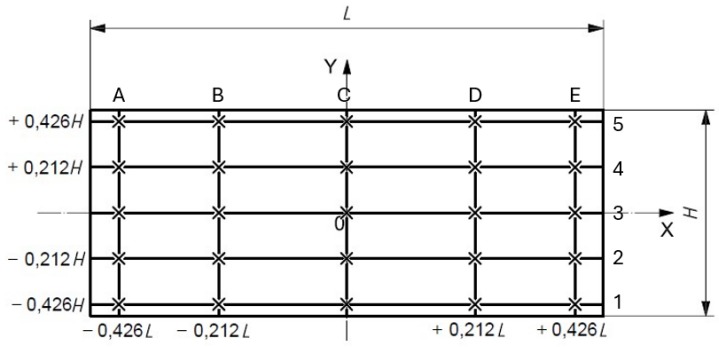

b) Points within the cross section.

Figure 3: Location of velocity measurements within the cross-section of the collector zone.

4.2 Uncertainty Calculation

The uncertainty in measuring dynamic pressure P_v comprises a systematic uncertainty from the instrument and a random component estimated using statistical methods. The total uncertainty u_{P_v} for each measurement is calculated as the root-sum-square of both components, as shown in Equation 10,

$$u_{P_v} = \sqrt{u_{P_{v,\text{sys}}}^2 + u_{P_{v,\text{rand}}}^2} \tag{10}$$

where $u_{P_{v,\text{sys}}}$ is the systematic component of the uncertainty, which in this case is 0.125 Pa, and $u_{P_{v,\text{rand}}}$ is the random component, estimated from the standard deviation of measurements taken at each point.

Since the velocity is derived from the pressure measurement, its uncertainty is calculated through uncertainty propagation of the formula used for the calculation. The uncertainty for each point is thus obtained using Equation 11,

$$u_v = \frac{1}{2}\sqrt{\frac{2}{\rho P_v}}u_{P_v} \tag{11}$$

where ρ is the air density, P_v is the dynamic pressure measured at the point, and u_{P_v} is the associated uncertainty in dynamic pressure at that point.

To calculate the uncertainty of the mean velocity value for the section, uncertainty propagation in the average calculation is applied, as shown in Equation 12,

$$u_{\bar{v}} = \sqrt{\frac{1}{N}\sum_{i=1}^{N} u_{v,i}^2} \tag{12}$$

where N is the number of measured points, in this case, 25, and $u_{v,i}$ is the uncertainty of each point.

Finally, the uncertainty in the calculated flow rate is also determined from uncertainty propagation, as shown in Equation 13,

$$u_Q = \sqrt{(A\,u_{\bar{v}})^2 + (\bar{v}\,u_A)^2} \tag{13}$$

where A is the cross-sectional area of the measured section, and u_A is its uncertainty, estimated from the measurement uncertainty of the tape measure used to record the section dimensions.

5 RESULTS AND DISCUSSION

Experimental results of velocity in the absorber sections and static pressure at some locations are presented for the empty kiln, setting the fans at an intermediate velocity ($40\,Hz$) through the variable frequency drive. Numerical results are presented in three steps. First, simulations of the empty dryer are performed and validated with experimental results. Second, the drying zone is simulated, including the wood stack (imposing a global volumetric flow rate), evaluating the quality of the mesh and the airflow behavior in the stack zone. Finally, the entire dryer is simulated, including the wood stack, setting the fan speed and verifying the operating conditions of pressure drop and volumetric flow. The latter are performed for the original conditions and for an alternative, which includes a blocking plate to eliminate air deviation around the woodpile.

5.1 Experimental results

The flow rate was measured for a typical operating point of the setup, assuming a constant air density throughout the test ($\rho = 1.2\,\mathrm{kg/m^3}$). Table 1 presents the measured dynamic pressure values at each point, along with the corresponding calculated velocities and uncertainties.

Table 1: Dynamic pressure, velocities, and uncertainties at various points in the cross-section of the collector zone.

Point	**Measurement**	P_v **(Pa)**	u_{P_v} **(Pa)**	v **(m/s)**	u_v **(m/s)**
A	1	12.36	0.9701	4.54	0.18
	2	10.68	1.0265	4.22	0.20
	3	7.41	1.5619	3.52	0.37
	4	3.94	1.4827	2.56	0.48
	5	1.30	0.7500	1.47	0.42
B	1	16.70	1.3341	5.28	0.21
	2	17.10	1.2074	5.34	0.19
	3	12.67	2.2325	4.60	0.40
	4	4.14	1.1094	2.63	0.35
	5	0.92	0.5562	1.24	0.37
C	1	6.21	0.8305	3.22	0.22
	2	10.61	1.3885	4.20	0.28
	3	7.99	1.3053	3.65	0.30
	4	4.00	1.5187	2.58	0.49
	5	1.52	0.6994	1.59	0.37
D	1	17.83	0.7548	5.45	0.12
	2	17.68	1.3637	5.43	0.21
	3	8.09	2.2035	3.67	0.50
	4	3.52	1.1160	2.42	0.38
	5	0.47	0.9875	0.88	0.93
E	1	18.20	1.2972	5.51	0.20
	2	19.17	1.9435	5.65	0.29
	3	12.72	2.0449	4.60	0.37
	4	6.93	1.1125	3.40	0.27
	5	2.74	1.1667	2.14	0.45

From the measured velocities, an average velocity $\bar{v}$ for the section was determined with an uncertainty $u_{\bar{v}}$.

Given the height $h = 0.24\,\mathrm{m}$ and width $w = 3.73\,\mathrm{m}$ of the section, its cross-sectional area results in $A = 0.895\,\mathrm{m^2}$. Using this value, the circulating flow rate $Q = 3.22\,\mathrm{m^3/\,s}$ was determined with uncertainty $u_Q = 2.15\%$.

Furthermore, velocities at the two locations in the drying zone L_1 and L_2 (shown in fig. 3-a) are presented in Table 2, together with their uncertainties.

Finally, pressure difference was measured between two locations before and after the fans, obtaining a value of approximately $50\,Pa$. Despite having high uncertainty —it was difficult to reach the measurement points and there is no certainty in the distance between them and the

Table 2: Measured velocities and uncertainties at different heights and locations.

Location	**Height (cm)**	v **(m/s)**	u_v **(m/s)**
L_1 (1 m)	10	0.53	0.38
	20	1.16	0.49
	30	2.13	0.36
	40	3.13	0.23
	50	3.83	0.20
L_2 (2 m)	10	1.35	0.37
	20	1.97	0.32
	30	2.65	0.30
	40	3.19	0.27
	50	3.71	0.14

fan inlet and outlet — this measurement is useful to have a hint on if there is some coincidence between reality, fan curves and simulation results.

5.2 Simulations of the empty dryer

This section presents a complete validation of the model against the experimental results. The dryer is empty and the fans are operated at 40 Hz, as in the experiment (as explained in section 4). Two types of mesh refinement are assumed. Figure 4 shows a geometric detail of the mesh. The structure cell was adopted with different levels of refinement in regions a, b, and c (see figure), as detailed in Table 3.

The results are shown in Figure 5 for the two vertical lines (at 1 and 2 meters from the collector outlet, as shown in Figure 3-a). The velocity in Line 1 shows a profile with a maximum speed of $4m/s$ near the floor, decreasing to zero at $0.5m$. Beyond this point the velocity reverses. The velocity in Line 2 (farther from the collector) shows a similar behavior to Line 1 but with a more diffused profile and a slightly lower maximum value.

The numerical results from the two evaluated meshes show very good agreement with the measurements. For Line 1, it can be observed that the point of maximum velocity is correctly captured by both meshes, with some discrepancies in the region above 0.3 meters. Both meshes slightly deviate from the experimental data between 0.2 and 0.4 meters, but the differences are within the expected errors for this type of analysis. In Line 2, both meshes show better agreement between 0.2 and 0.5 meters, while the region near the floor, where the maximum velocity is reached, is better represented by the finer mesh.

In Figure 5-c the mean velocity vector field is shown in a vertical plane intersecting lines 1 and 2. A large recirculation vortex is observed, as mentioned above. In addition, a second recirculation vortex is detected near the drying zone inlet (collector zone outlet). It can be seen how the main flow travels near the ground, from the solar collector outlet through the drying zone until it almost reaches the opposite wall, where it abruptly heads vertically toward the fan return plenum.

Figure 6 shows the velocities obtained in the cross section of measurement of the collector zone (see figure 3), together with the corresponding experimental measurements. Lines A and E are close to the edges and line C is in the center of the channel. The velocity profiles show a distribution with its maximum close to the collector plate ($y = 0m$). This is caused by the horizontal wooden beams at the top of the channel (supporting the polycarbonate cover; see

Mesh	N	a	b	c	Mean y^+
-	-	(mm)	(mm)	(mm)	-
Mesh1	1.36×10^6	20	26.4	60	131
Mesh2	8.12×10^6	10.5	11.3	15.3	84

Table 3: Mesh parameters in the solar wood dryer.

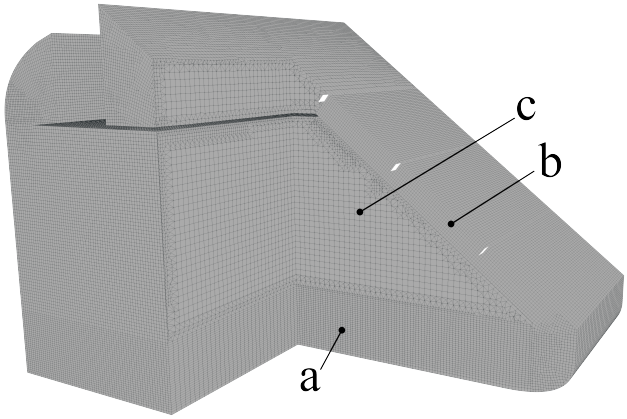

Figure 4: Wood dryer mesh details.

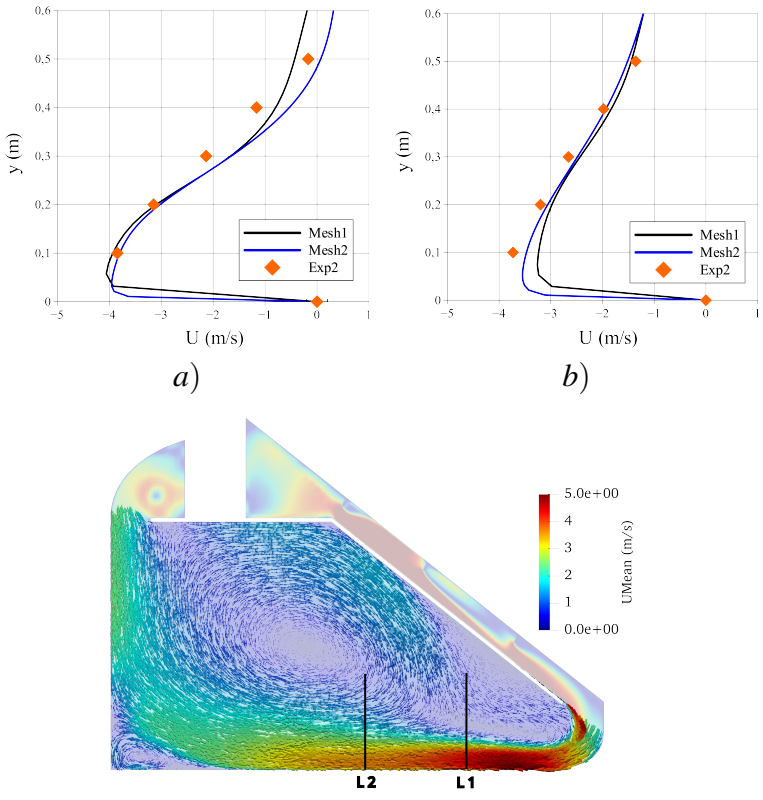

Figure 5: Mean velocity field: a) Line 1 (1m), b) Line 2 (2m) and c) Vector field a vertical plane.

Fig. 1), which prevent the flow from developing near the cover and cause it to develop near the lower surface (absorber plate).

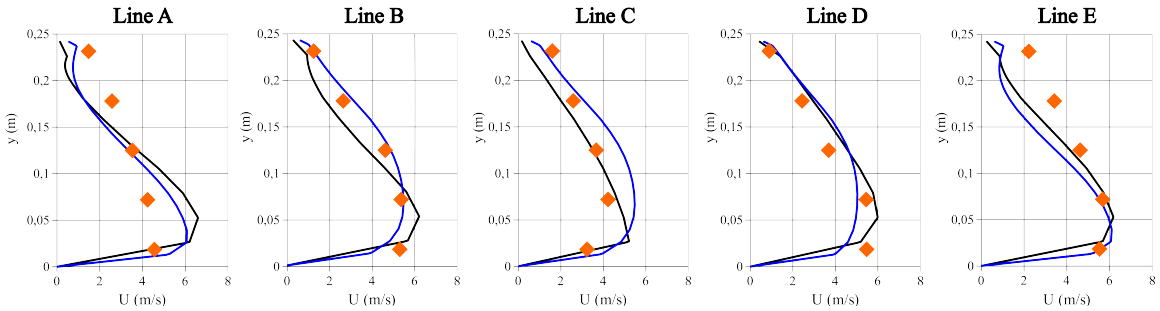

Figure 6: Velocity profile in five lines in the collector zone. Black curve: Mesh 1

While numerical and experimental results show similar trends and good agreement in general, the velocity profiles show some discrepancies in certain areas. It should be noted that the flow distribution in the CFD simulations is quite symmetric between the two ends of the duct. In contrast, the experimental data show a clear asymmetry near the edges (lines A and E). The maximum velocity in line A is about 5 m/s, while in line E it is about 6 m/s. This asymmetry might be attributed to differences between the fans or construction asymmetries that where not evident and therefore no taken into account in the simulations.

In terms of the comparison between meshes 1 and 2, the results show great agreement between the extremes while in the central zone mesh 1 shows a profile somewhat distant from the experiment; however, the results are acceptable taking into account some construction imperfections, material irregularities, and surface roughness not included in the CFD model.

5.3 Wood stack and drying zone simulations

In this section, a numerical analysis of the drying zone including the wood stack is presented. A mesh quality assessment is performed and the behaviour of the airflow is evaluated. Some considerations are done regarding flow homogeneity and the "efficiency" of the air circulation, i.e. the portion of air effectively passing through the wood stack.

Figure 7-a shows the drying zone geometry schematically, as well as a detail on the wood stack zone. The latter consists of a $2.5 \times 1.8 \times 1.9m$ conventional structure stack (see Figure 7-b). As can be seen, the boards are arranged horizontally in layers, each supported by three "stickers" (long strips of wood) placed perpendicular to the long side of the boards (longitudinally in the direction of airflow), to allow airflow between the boards.

Table 4 summarizes the parameters of the three tested meshes. To take as references, the number of cells for the edges n_1 and n_2 (shown in fig. 7-b) are presented. The rest of the domain has a mesh density that keeps the proportionality of the parameters n_1 and n_2. The simulations were carried out imposing the design volumetric flow rate ($3.2 m^3/s$) until reaching the steady state, and then a time average of the volumetric flow rate for each layer between tables is monitored (in fig. 7-a, M1 to M15 indicate each layer, while M indicates the zone where the air flow may bypass the stack, i.e. the sides and above).

Figure 8-a shows results of volumetric flow rate in all the stack layers. The mesh validation demonstrates good mesh convergence. As shown in the figure, mesh 0 shows slight discrepancies compared to meshes 1 and 2. Furthermore, a heterogeneous flow distribution is observed between stack layers. In addition, the flow presents a reverse recirculation in the upper half of

Table 4: Mesh parameters in the Pile.

Mesh	$n1$	$n2$	N	Mean y^+	Min y^+	Max y^+
Mesh0	26	3	1.056×10^6	24.41	1.89	134
Mesh1	50	6	2.830×10^6	17.39	0.91	75.4
Mesh2	75	12	7.924×10^6	8.6	0.51	38.6

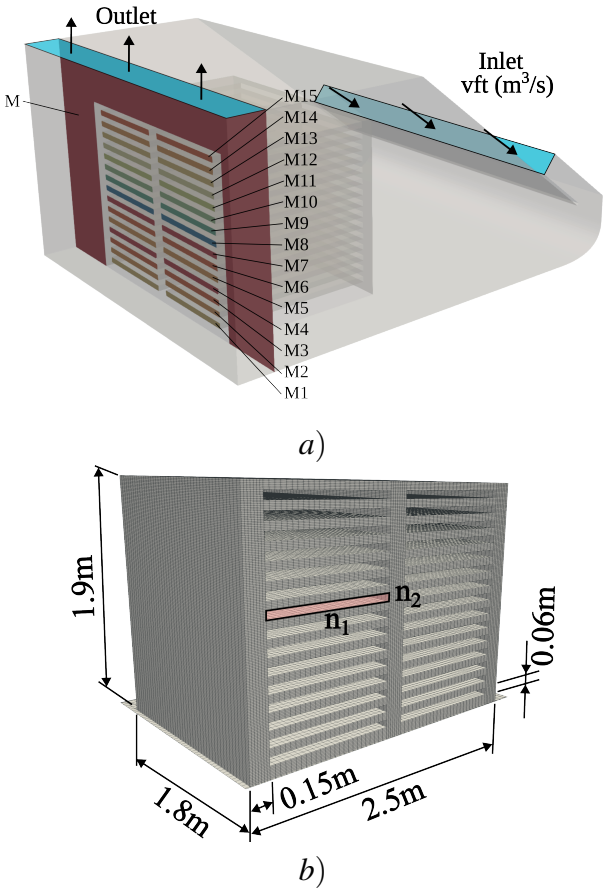

Figure 7: Mesh assessment of the drying zone: a) Computational domain, b) Mesh detail of the pile.

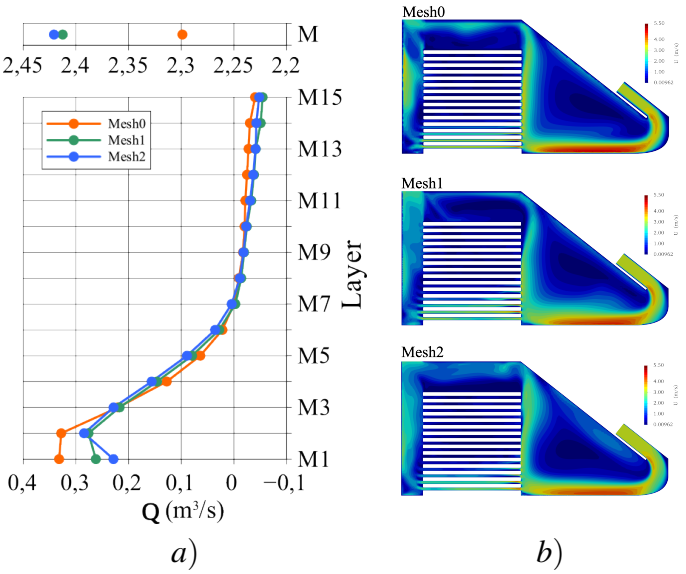

Figure 8: Wood pile validation results: a) Volumetric flow rate in the layers, b) Velocity contour in a vertical plane.

the stack (layers M8 to M15). The layers close to the ground show the highest flow rate, as the flow from the solar collector is mainly directed close to the ground.

The most important aspect of this analysis is the proportion of flow that enters between the boards and the flow that bypasses the woodpile. As shown in the figure, the flow rate surrounding the pile varies between 2.3 and 2.43 m³/s for the three cases. This indicates that less than 30% of the flow passes through the wood pile, while more than 70% of the flow bypasses it.

Regarding the velocities of the flow between boards, it is observed that the maximum velocities are close to $2.4 m/s$ (in the lowest layer —M1) and only layers M1 to M5 have velocities higher than $0.5 m/s$ (which could be considered typical), with most of the other layers presenting negative velocities (reverse flow). Figure 8-b shows the velocity contours in a vertical plane that cuts through the pile. As shown in the figure, the velocity profiles are similar for the three meshes.

5.4 Full dryer simulations

In this section, the global model is analyzed taking into account the wood stack, the solar collector, and the fans operating at 40 Hz. For this case, appropriate levels of mesh refinement are used, according to the previous mesh assessment phases.

Figure 9 shows the streamlines in the wood dryer (a perspective and a lateral view). As can be observed, the flow driven by the fans passes through the solar collector zone, encountering three obstructions (wooden beams at the top of the channel supporting the polycarbonate cover) along its path. This generates high-velocity fluctuations and significant turbulence. Then, in the drying zone, most of the airflow remains near the floor until it encounters the stack of wood, creating a large recirculation with a sizable vortex. As noted in the previous section, most of the air bypasses the wood stack. Furthermore, as was observed in Figure 8 the air flow in the upper layers is reversed, and the central layers present almost zero flow.

From the point of view of heat transfer between the collector plate and the air, the turbulent fluctuations generated by the collector wooden boards improve the energy transfer while

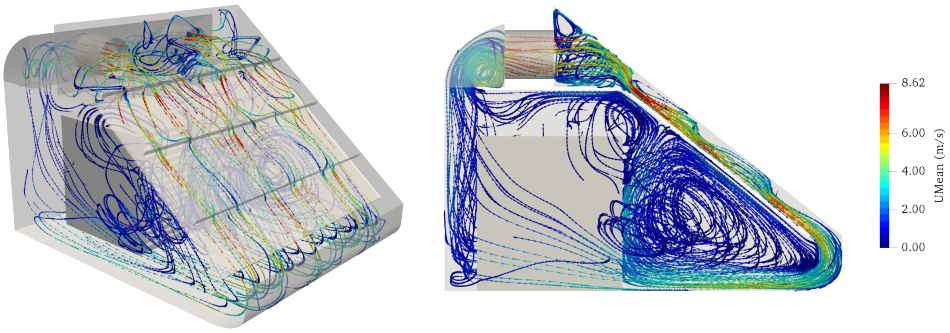

Figure 9: Streamlines in the solar wood dryer.

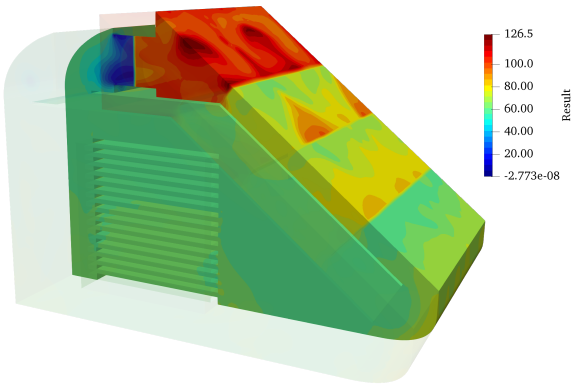

Figure 10: Pressure distribution in a vertical plane cutting a fan.

increasing the pressure drop.

The pressure along the wood dryer is shown in Figure 10. Each fan reaches an operating point with a volumetric flow rate of $1.72 m^3/s$ and a pressure jump of $79.5 Pa$. It can be observed that the highest pressure changes are located in the fan return plenum, the supply plenum and the solar collector area. The pressure changes in the drying area are much smaller and almost negligible. It should be noted that the observed pressure changes are not only due to "pressure losses", but also to contractions and expansions (in the plenums). Overall, the main pressure losses in the circuit seem to occur in the plenums and the solar collector areas, where high velocities and abrupt changes occur.

All the above analyses show that the original dryer (without modifications) operates inefficiently both in terms of flow homogeneity along the stack and flow deviation, despite the high volumetric flow rate of the fans. These effects lead to slow and heterogeneous drying and therefore to defects. For this reason, an additional analysis is carried out for a case where the side and top spaces of the wood-stack are blocked.(Case 1 in Fig. 11).

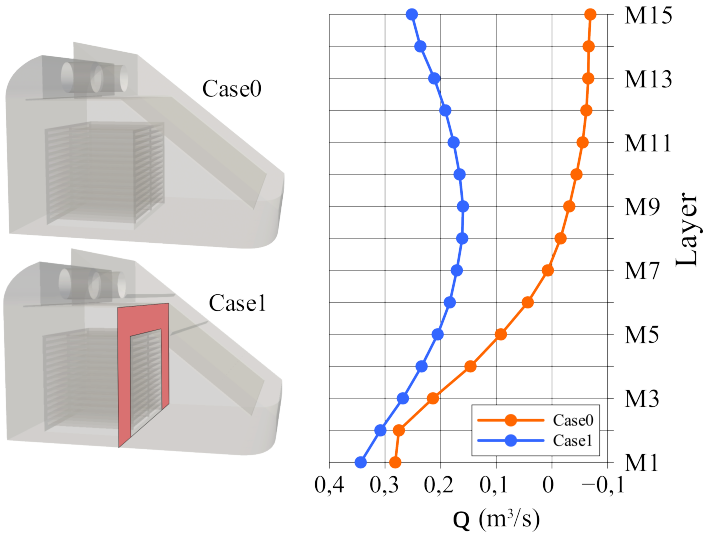

Figure 11: Left: sketches of Cases 0 and 1. Right: results of flow through the wood stack layers for both cases.

Figure 11 shows the comparison between the flow distribution in the pile gaps for the case without the vertical plate (Case 0) and with plate (Case 1). As can be seen, the incorporation of the plate increases the flow rate significantly, even avoiding the flow in the opposite direction for the plates M8-M15. Due to the restriction imposed by the plate, the global volumetric flow is reduced 3.3% approximately respect to the case without plate.

In addition to the fact that the flow between the boards is greater in Case 1 and does not show regions of reversed or stagnant flow, the flow homogeneity is also improved. Case 0 shows min/max flow rate deviations of up to 6.17% (M5) and 187.8% (M1) from the general average taken into account the absolute values of the mass flow rate (around $0.098 m^3/s$). In contrast, the redesigned case (Case 1) exhibits maximum deviations of 2.93% (M13) and 57.6% (M1) from an average of $0.22 m^3/s$. Regarding airflow velocities, Case 1 shows values in the range $1.3 - 2.8 m/s$, which could be considered acceptable. This demonstrates that inclusion of a vertical plate improves the homogeneity of the flow between layers, not yet being entirely acceptable, eliminating the air bypass through the sides and above the stack and therefore increasing the velocities in the channels.

Finally, Figure 12 shows the fan curve (at 40 Hz) together with the system curve for the empty dryer and the results for both Cases 0 and 1 (both including the stack). The experimental measurement (without the stack) of pressure difference between inlet and outlet of the fans was also included. It should be noted that due to the geometry of the zone where the fans are located, pressure measurements were taken at a considerable distance from the suction side. As shown in Figure 10, the pressure changes abruptly near the fan, which would explain the lower pressure jump compared to the model results.

Another important aspect of the results in Figure 12 is the difference in operating points between Cases 0 and 1. As previously analyzed, the highest pressure loss occurs in the upper part of the dryer, and not in the drying zone. This aspect is highly relevant because the operating flow rate of the fans is almost not affected by the incorporation of the vertical plate in Case 1. Moreover, the redesign does not lead to an increase in the system's electrical consumption.

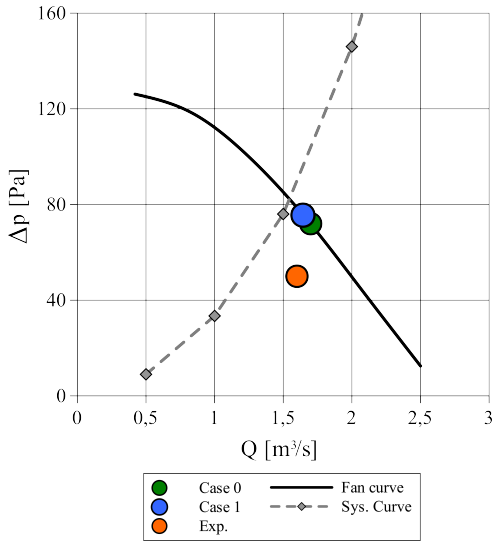

Figure 12: Fan (at 40 Hz) and system (without the stack) pressure - flowrate curves, experimental measurement (without stack) and results of simulated Cases 0 and 1 (with stack).

6 CONCLUSIONS

This study deals with a comprehensive investigation of an Oxford-type solar timber kiln, employing both experimental measurements and numerical simulations. As highlighted in the literature, the main challenge in this type of kiln, as well as in industrial kilns, is ensuring homogeneous drying across the timber stack. For this reason, this work focuses on the following key objectives: studying the fluid dynamics inside the kiln by validating results against experimental data, analyzing efficiency in terms of flow homogeneity through the timber stack and airflow deviations (bypass), and evaluating potential modifications to the kiln design. The computational simulation results showed good agreement with the experimental data and demonstrated a high level of mesh independence. Results revealed that in the original model, with the timber stack positioned in the central zone of the kiln and without any blocking device around the stack, the performance in terms of airflow homogeneity is deficient for ensuring uniform drying. The results of including a blocking device, eliminating the bypass of air around the stack, not only improve the dryer effectiveness but also shows significant improvements in terms of

airflow distribution within the timber stack, with a minimal impact on the volumetric flow rate provided by the fans.

The results of the computational simulation showed good agreement with the experimental data and demonstrated a high level of mesh independence. The results revealed that, in the original model, with the wood pile located in the central zone of the kiln and without any blocking devices around it, most of the airflow is diverted around the pile, and there is also a very heterogeneous flow distribution within it. The inclusion of a blocking device, which eliminates air bypass around the chimney, not only improves the efficiency of the dryer but also shows significant improvements in the airflow distribution within the wood pile, with minimal impact on the volumetric flow rate.

In the future, the model could be used to propose other design improvements, such as the inclusion of flow deflectors to improve flow homogeneity between tables. Also of interest is the determination of thermal aspects, such as convective heat and mass transfer coefficients, for use in simplified zero- or one-dimensional models.

ACKNOWLEDGEMENTS

The authors would like to thank ANPCyT (grant PICT 2019 - 0375), CONICET (PIP 11220210100709CO) and Universidad Nacional del Litoral. Diego Passarella and the team from Centro Universitario de Tacuarembó, UdelaR,

REFERENCES

Bekkioui N. Performance comparison and economic analysis of three solar dryer designs for wood using a numerical simulation. *Renewable Energy*, 164:815–823, 2021. ISSN 0960-1481. doi:https://doi.org/10.1016/j.renene.2020.09.126.

Haque M. and Langrish T. Stack-wide effects in the modeling of solar kilns for drying timber. *Drying Technology*, 19(1):99–114, 2001.

Hasan M. and Langrish T.A. Numerical simulation of a solar kiln design for drying timber with different geographical and climatic conditions in australia. *Drying Technology*, 32(13):1632–1639, 2014.

Hasan M. and Langrish T.A. Performance comparison of two solar kiln designs for wood drying using a numerical simulation. *Drying Technology*, 33(6):634–645, 2015.

Herritsch A., Dronfield J., and Nijdam J.J. Intermittent and continuous drying of red beech timber from the green condition. *Drying Technology*, 28(2):269–277, 2010. doi:10.1080/07373930903530287.

Khater H.A., Helwa N.H., Enayet M.M., and Hashish M.I. Optimization of solar kiln for drying wood. *Drying Technology*, 22(4):677–701, 2004. doi:10.1081/DRT-120034257.

Lamrani B., Bekkioui N., Simo-Tagne M., and Ndukwu M.C. Recent progress in solar wood drying: An updated review. *Drying Technology*, 41(5):605–627, 2023.

Launder B.E. and Spalding D.B. The numerical computation of turbulent flows. In *Numerical prediction of flow, heat transfer, turbulence and combustion*, pages 96–116. Elsevier, 1983.

Ledig S.F., Paarhuis B., and Riepen M. Chapter 13 - airflow within kilns. In P. Perré, editor, *Fundamentals of wood drying*, pages 291–332. A.R.BO.LOR, ENGREF, 2007.

Ltd T.O.F. OpenFOAM v8. 2020.

Menter F.R., Kuntz M., Langtry R., et al. Ten years of industrial experience with the sst turbulence model. *Turbulence, heat and mass transfer*, 4(1):625–632, 2003.

Perré P. *Fundamentals of wood drying*. A.R.BO.LOR ENGREF, 2007.

Perré P. and Keey R.B. Chapter 40 - drying of wood: Principles and practices. In *Handbook of Industrial Drying, 4th ed.*, pages 373–402. CRC Press: Boca Raton, Florida, 2014. ISBN 9780429169762.

Prakash O. and Kumar A. *Solar drying technology: concept, design, testing, modeling, economics, and environment*. Springer, 2017.

Prins A. Oxford solar kiln research: 1978-1979. *The Commonwealth Forestry Review*, pages 187–196, 1981.

VEINSA. VEINSA. 2024.

Wilcox D.C. Formulation of the kw turbulence model revisited. *AIAA journal*, 46(11):2823–2838, 2008.

Zhao J. and Cai Y. A comprehensive mathematical model of heat and moisture transfer for wood convective drying. *Holzforschung*, 71(5):425–435, 2017.